Study of the Spin−Spin Interactions between the Metal Centers of *Desulfovibrio gigas* Aldehyde Oxidoreductase: Identification of the Reducible Sites of the [2Fe-2S]$^{1+,2+}$ Clusters

Claude More,[‡] Marcel Asso,[‡] Guy Roger,[‡] Bruno Guigliarelli,[‡] Jorge Caldeira,[§,||] José Moura,[§] and Patrick Bertrand*[,‡]

Laboratoire de Bioénergétique et Ingénierie des Protéines, UPR 9036 CNRS and Université de Provence, 31 Chemin Joseph Aiguier, 13402 Marseille, France, Requimte, Centro de Quimica Fina e Biotecnologia, Faculdade de Ciências e Tecnologia, Universidade Nova de Lisboa, 2829-515 Caparica, Portugal, and Instituto Superior de Ciências da Saùde-Sul, 2829-516 Caparica, Portugal

Received May 27, 2005; Revised Manuscript Received June 28, 2005

ABSTRACT: The aldehyde oxidoreductase from *Desulfovibrio gigas* belongs to the family of molybdenum hydroxylases. Besides a molybdenum cofactor which constitutes their active site, these enzymes contain two [2Fe-2S]$^{2+,1+}$ clusters which are believed to transfer the electrons provided by the substrate to an acceptor which is either a FAD group or an electron-transferring protein. When the three metal centers of *D. gigas* AOR are simultaneously paramagnetic, splittings due to intercenter spin−spin interactions are visible when the EPR spectra are recorded at low temperatures. By studying quantitatively these interactions with a model based on the X-ray crystal structure, which takes into consideration the interactions between the magnetic moments carried by all the metal sites of the system, it is possible to determine the location of the reducible sites of the [2Fe-2S] clusters. When combined with the electron-transfer pathways proposed on the basis of the X-ray crystal structure, the results provide a detailed description of the electron-transfer system of *D. gigas* AOR.

Some molybdenum-containing enzymes catalyze the oxidative hydroxylation of aldehydes and aromatic heterocycles. A well-known member of this family is the eucaryotic protein xanthine oxidase, but related enzymes such as aldehyde oxidoreductases and CO dehydrogenases have been found in bacteria (*1*). Spectroscopic studies have shown that, besides the molybdenum cofactor which constitutes their active site, these proteins contain two [2Fe-2S]$^{1+,2+}$ clusters together with a FAD[1] group in enzymes where the electrons are delivered to a second substrate. The highly homologous amino acid sequences of all molybdenum hydroxylases are indicative of a very similar arrangement of their cofactors. This was confirmed by the recent resolution of the X-ray crystal structures of several enzymes of this family, the AOR from *Desulfovibrio gigas* (*2*), the CO dehydrogenases from *Oligotropha carboxidovorans* (*3*) and *Hydrogenophaga pseudoflava* (*4*), the bovine milk xanthine dehydrogenase and xanthine oxidase (*5*), and the xanthine dehydrogenase from *Rhodobacter capsulatus* (*6*). This arrangement strongly suggests that, in all these enzymes, electron transfer between the molybdenum center and the physiological acceptor or the FAD group is mediated by the FeS centers (*7*). In the case of xanthine oxidase and xanthine dehydrogenase, kinetic studies have shown that reduction of the molybdenum center by xanthine is the rate-limiting step in enzyme turnover (*8*), and that the FeS centers are involved in the fast electron exchange between the molybdenum center and the FAD (*9*, *10*). However, the values of the midpoint potentials of the FeS centers vary greatly among the class of molybdenum hydroxylases (*11*−*13*), and their ordering along the electron-transfer system is not always favorable to a quasi-unidirectional transfer. An extreme situation is found in the case of CO dehydrogenase where the Mo(VI/V), Mo(V,IV), FeSI and FeSII midpoint potentials at pH 7.2 are equal to − 90 mV, −380 mV, − 40 mV, and −270 mV, respectively (Gremer, L., Meyer, O., Guigliarelli, B., Bertrand, P., unpublished results).

Besides thermodynamic factors, the efficiency of an electron-transfer system is determined by the electron-transfer capability of the pathways connecting the redox centers. Detailed pathways have already been proposed in the case of *D. gigas* AOR, for which a high-resolution crystal structure is available (*2*, *14*). However, owing to the spatial extent of the cofactors, the efficiency of these pathways can be evaluated only if the sites where a redox change takes place are accurately known. Mössbauer experiments have shown that the [2Fe-2S] clusters of *D. gigas* AOR possess well-defined reducible sites (*15*), but their location in the clusters is presently unknown.

In the reduced form, the [2Fe-2S] centers of molybdenum hydroxylases exhibit distinct EPR spectra. The less aniso-

* To whom correspondence should be addressed. Phone: (33) 4 91 16 44 47. Fax: (33) 4 91 16 45 78. E-mail: bertrand@ibsm.cnrs-mrs.fr.
[‡] UPR 9036 CNRS and Université de Provence.
[§] Universidade Nova de Lisboa.
[||] Instituto Superior de Ciências da Saùde-Sul.

[1] Abbreviations: AOR, aldehyde oxidoreductase; FAD, flavin adenin dinucleotide; EPR, electron paramagnetic resonance; ENDOR, electron nuclear double resonance.

10.1021/bi0510025 CCC: $30.25
Published on Web 08/06/2005

tropic one, called signal I, is characterized by g values, line widths, and a relaxation behavior which are similar to those of the $g_{av} \approx 1.96$ type signals of $[2Fe\text{-}2S]^{1+}$ centers in ferredoxins, whereas the more anisotropic signal II often exhibits unusual properties (*16*). When *D. gigas* AOR is prepared in a redox state such that the three metal centers are paramagnetic, splittings due to intercenter spin−spin interactions are visible at low temperatures in the Mo(V) spectrum and in signal I. We have established previously that the temperature dependence of the shape of the split Mo(V) spectrum is governed by the spin−lattice relaxation time T_1 corresponding to signal I, which demonstrates that signals I and II originate from the proximal and distal centers, respectively (*16*). Other methods lead to the same assignment in the case of xanthine oxidase (*17*, *18*), CO dehydrogenase (*19*), and other enzymes of this family (*20*−*22*). The quantitative study of intercenter spin−spin interactions can also be used to determine the location of the reducible site in [2Fe-2S] centers. This is because of the fact that, when an FeS cluster interacts magnetically with another paramagnetic center, the shape of the interaction EPR spectrum depends not only on the geometry of the system but also on the valence state of the Fe ions in the cluster (*18*, *23*). This property was used to explain why no dipolar coupling effect is detected in the EPR spectrum of the NADH-reduced state of *Pseudomonas cepacia* phthalate dioxygenase reductase, in which a [2Fe-2S] center and a flavin ring separated by a center-to-center distance of 12 Å are both paramagnetic (*24*). In the present work, this property is used to identify the reducible sites of the two [2Fe-2S] centers in *D. gigas* AOR.

EXPERIMENTAL PROCEDURES

Sample Preparation. The samples of *D. gigas* AOR used in this study have been described previously (*16*). The spin−spin interactions between the Mo(V) center and the proximal $[2Fe\text{-}2S]^{1+}$ cluster were analyzed by using the slow-type Mo(V) signal which is very sharp and uncomplicated by resolved hyperfine interactions (*25*). This signal was generated by reducing the enzyme solution, buffered in ^2H_2O, with sodium dithionite. Its intensity was found to be substoichiometric, as observed in other molybdenum hydroxylases (*21*, *25*).

The samples of milk xanthine oxidase used in this study have been described previously (*18*).

EPR Spectroscopy. X-band EPR spectra were recorded on a Bruker ESP 300E spectrometer. Samples were cooled with an Oxford Instrument ESR 900 cryostat fitted with an ITC 503 temperature controller. Q-band spectra were recorded by using a ER051QG microwave bridge and a CF935 cryostat.

Analysis of the Spin−Spin Interactions. The redox potentials of the FeS centers and of the molybdenum center of *D. gigas* AOR are such that the effects of the intercenter spin−spin interactions are most visible in the EPR spectrum when the three centers are simultaneously paramagnetic. In this three-center system, the analysis of the spin−spin interactions is facilitated by the structural arrangement of the centers (Figure 1). As mentioned above, the splitting of the Mo(V) spectrum is due to the spin−spin interactions with the proximal $[2Fe\text{-}2S]^{1+}$ center. Since the proximal $[2Fe\text{-}2S]^{1+}$ center interacts magnetically with both the Mo(V) center and the distal $[2Fe\text{-}2S]^{1+}$ center, the origin of the split signal I is less clear. However, the fact that this signal is observed in spectra where the intensity of the Mo(V) signal is greatly substoichiometric demonstrates that it arises from the spin−spin interactions with the distal $[2Fe\text{-}2S]^{1+}$ center.

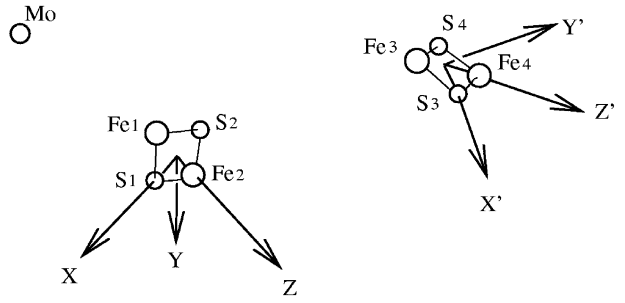

FIGURE 1: Relative arrangement of the metal centers given by the X-ray crystal structure of *D. gigas* AOR. The Fe atoms are numbered according to increasing distances from the molybdenum center. Fe_1 is coordinated by Cys 100 and Cys 139, Fe_2 by Cys 103 and Cys 137, Fe_3 by Cys 40 and Cys 45, Fe_4 by Cys 48 and Cys 60 (see also Figure 6). The axes (X, Y, Z) and (X',Y', Z') used in the calculation of the interaction spectra are defined in the text.

The numerical simulation of interaction spectra was based on a local spin model which goes beyond the point dipole approximation by considering explicitly the dipolar interactions between the magnetic moments carried by all the metal sites of the system (*18*). This allows the valence state of the metal ions to be determined from the numerical simulation of interaction spectra recorded at different microwave frequencies. In the case of *D. gigas* AOR, the arrangement of the two [2Fe-2S] clusters is such that the four intercenter iron-to-iron distances fall in the narrow range 12.2 to 15 Å. This rather symmetrical arrangement is not favorable for the determination of the valences of the four Fe ions from the sole study of their spin−spin interactions. Therefore, the valence state of the Fe ions of the proximal $[2Fe\text{-}2S]^{1+}$ cluster was first deduced from the simulation of the split Mo(V) spectrum, and the valence state of the Fe ions of the distal $[2Fe\text{-}2S]^{1+}$ cluster was subsequently deduced from the analysis of the spin−spin interactions between the two clusters.

The Mo−Fe and Fe−Fe distances needed in the calculation were taken from the crystal structure of *D. gigas* AOR at 1.28 Å resolution (*14*). In the following, the **g** tensors of the Mo(V) center and of the proximal and distal $[2Fe\text{-}2S]^{1+}$ clusters are noted $\mathbf{g}_m$, $\mathbf{g}_p$, and $\mathbf{g}_d$, respectively. Their principal values were deduced from numerical simulations of frozen solution spectra in which the effect of the spin−spin interactions is not visible. Spectra of this kind were obtained either by preparing the sample in an appropriate redox state or by raising the temperature so that the effects of the spin−spin interactions are averaged out (see below). The orientation of the three **g** tensors with respect to the molecular structure was left adjustable. In the case of the proximal cluster, this orientation was specified with respect to a reference system (X, Y, Z) centered on the midpoint of Fe_1Fe_2. The Z axis was taken to be along the Fe_1Fe_2 direction, and X was chosen so as to put the bridging sulfur S_1 in the XZ plane (Figure 1). A system (X', Y', Z') centered on the midpoint of Fe_3Fe_4 was defined in the same way for the distal center. The orientation of the $\mathbf{g}_m$ and $\mathbf{g}_p$ axes (x, y, z, with $g_x < g_y < g_z$) with respect to (X, Y, Z) was specified by two

Table 1: *g* Values and Line Width Parameters (Dimensionless) Deduced from the Numerical Simulations of the Unsplit Slow-Type Mo(V) Signal, Signal I, and Signal II Shown in Figure 2

	$g_{x,y,z}$	$\sigma_{x,y,z}$ (in units of 10^{-4})
Mo(V)	1.9581, 1.9678, 1.9703	15, 14, 15 (X-band) 5.5, 5.6, 6.0 (Q-band)
signal I	1.9183, 1.9360, 2.020	57, 38, 50 (X-band) 47, 26, 32 (Q-band)
signal II	1.8963, 1.9687, 2.0613	137, 110, 145 (X- and Q-bands)

sets of Euler angles noted (*a*, *b*, *c*) and (α, β, γ), respectively. Likewise, the orientation of the $\mathbf{g}_d$ axes (*x*, *y*, *z*, with $g_x < g_y < g_z$) with respect to (*X*′, *Y*′, *Z*′) was specified by the set (α', β', γ'). The sensitivity of calculated spectra with respect to the orientation of $\mathbf{g}_p$ and $\mathbf{g}_d$ was studied by considering the 6 configurations for which the $\mathbf{g}_p$ axes are parallel to (*X*, *Y*, *Z*) and the 6 configurations for which the $\mathbf{g}_d$ axes are parallel to (*X*′, *Y*′, *Z*′). The values of α, β, γ, α', β', γ' were therefore restricted to 0° and 90°. The **g** tensors of the ferric and ferrous sites of the $[2Fe\text{-}2S]^{1+}$ clusters, which are needed in calculations based on the local spin model (*18*), were deduced from $\mathbf{g}_p$ and $\mathbf{g}_d$ by using $\mathbf{g} = {}^7/_3\mathbf{g}_1 - {}^4/_3\mathbf{g}_2$, where $\mathbf{g}_1$ and $\mathbf{g}_2$ are the ferric and ferrous **g** tensors, respectively. The $\mathbf{g}_1$ and $\mathbf{g}_2$ axes were assumed to be parallel, and the principal values of $\mathbf{g}_1$ were taken equal to $g_{1x} = 2.015$, $g_{1y} = 2.034$, $g_{1z} = 2.030$ (*18*).

Besides dipolar terms, the spin−spin interactions between two paramagnetic centers contain exchange terms which can be written in the form of a single Heisenberg Hamiltonian, even in the case of polynuclear centers (*18*). The exchange interactions between the Mo(V) center and the proximal $[2Fe\text{-}2S]^{1+}$ center were described by $J_{mp}\mathbf{S}_m\cdot\mathbf{S}_p$ and those between the proximal and distal $[2Fe\text{-}2S]^{1+}$ centers by $J_{pd}\mathbf{S}_p\cdot\mathbf{S}_d$. The line width of calculated spectra was treated by a *g*-strain procedure, as previously described (*18*). The convergence of the spectral simulations was ensured by using a regression procedure (*23*).

RESULTS

g Values and Line Width Parameters. When the Mo(V) signal is recorded at low temperatures, the effects of the spin−spin interactions between the Mo(V) center and the proximal $[2Fe\text{-}2S]^{1+}$ center are visible at both X- and Q-bands (*16*). Upon raising the temperature, the splittings progressively disappear due to the shortening of the spin−lattice relaxation time T_1 of the proximal cluster, until unsplit signals are finally observed above about 100 K (*16*). The *g* values and line width parameters of the Mo(V) signal were deduced from the numerical simulation of these unsplit signals by using the procedure described in ref 18. The best fits, which were obtained with the sets of parameters reported in Table 1, are shown in Figure 2a,b.

Determination of the *g* values and line width parameters of the noninteracting $[2Fe\text{-}2S]^{1+}$ clusters requires the numerical simulation of a spectrum arising from molecules in which a single cluster is paramagnetic. This was achieved by taking a sample at the very beginning of a reductive redox titration, carried out with sodium dithionite as reductant. Since the midpoint potential of the distal center is more positive than that of the proximal center (*13*), the number of molecules in which the distal center is paramagnetic is larger than that in which the proximal center is paramagnetic.

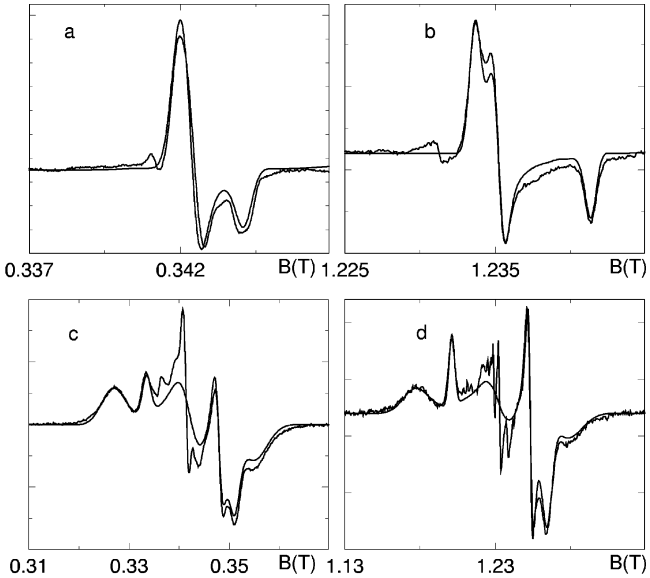

FIGURE 2: Unsplit slow-type Mo(V) signal, signal I and signal II of *D. gigas* AOR recorded at X- and Q-bands. (a,b) Unsplit slow-type Mo(V) signal recorded at X- and Q-bands. Experimental conditions: X-band, temperature 150 K, microwave frequency 9.4302 GHz, power 4 mW, modulation frequency 3.3 kHz, modulation amplitude 0.2 mT; Q-band, temperature 80 K, microwave frequency 33.98 GHz, power 0.1 mW, modulation frequency 12 kHz, modulation amplitude 0.2 mT. The best fit was obtained with the parameters reported in Table 1. (c,d) EPR spectra displayed at X- and Q-bands by *D. gigas* AOR when signal I and signal II are not perturbed by spin−spin interactions. Experimental conditions: X-band, temperature 8 K, microwave frequency 9.4280 GHz, power 10 μW, modulation frequency 2.9 kHz, modulation amplitude 1 mT; Q-band, temperature 40 K, microwave frequency 33.84 GHz, power 0.1 mW, modulation frequency 10 kHz, modulation amplitude 1 mT. These spectra were simulated by adding two components characterized by the parameters reported in Table 1. The stoichiometry of signal I and signal II was 1:1.4.

Therefore, the intensity of signal II is larger than that of signal I (Figure 2c,d). The spectrum was simulated by adding two nonstoichiometric components characterized by the *g* values and line width parameters given in Table 1.

Spin−Spin Interactions between the Mo(V) Center and the Proximal $[2Fe\text{-}2S]^{1+}$ Center of D. gigas AOR. The X-band and Q-band split Mo(V) signals are shown in Figure 3. Their main features could be reproduced by considering only the exchange term $J_{mp}\mathbf{S}_m\cdot\mathbf{S}_p$ of the spin−spin interactions with $|J_{mp}| = 1.2 \times 10^{-3}$ cm^{-1} (Figure 3a,b). In order to improve the fit, the dipolar terms were "turned on" with the two possible assignments Fe_1 = Fe(III) and Fe_1 = Fe(II). For each assignment, the six orientations of the principal axes of the $\mathbf{g}_p$ tensor with respect to (*X*, *Y*, *Z*), defined in Experimental Procedures, were tested. The four parameters involved in the fitting procedure were therefore the (*a*, *b*, *c*) angles which specify the orientation of the tensor $\mathbf{g}_m$ of the Mo(V) center with respect to (*X*, *Y*, *Z*) and the exchange parameter J_{mp}. The best simulations of the X-band and Q-band spectra given by the assignments Fe_1 = Fe(III) and Fe_1 = Fe(II), which were obtained with the parameters quoted in Table 2, are shown in Figure 3c,d and Figure 3e,f, respectively. With the assignment Fe_1 = Fe(III), only one orientation of the $\mathbf{g}_p$ tensor gave a roughly acceptable fit, whereas with Fe_1 = Fe(II) equivalent fits were obtained with the six tested orientations (Table 2). Although the two assignments lead to very similar simulations at Q-band (Figure

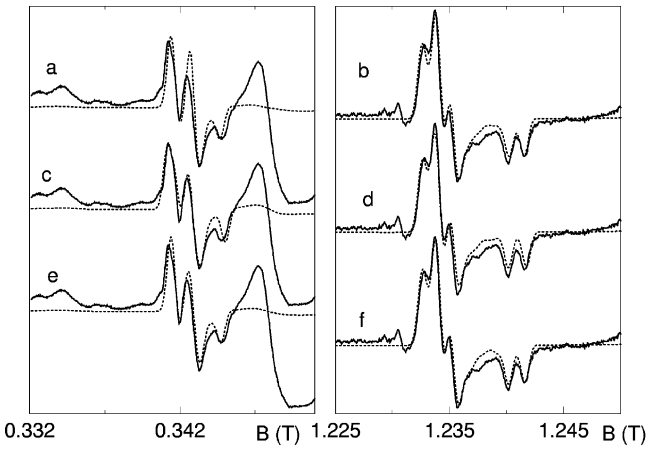

FIGURE 3: Split slow-type Mo(V) signal of *D. gigas* AOR recorded at X- and Q-bands. Experimental conditions: X-band, temperature 8 K, microwave frequency 9.4302 GHz, power 40 μW, modulation frequency 3.32 kHz, modulation amplitude 0.2 mT; Q-band, temperature 30 K, microwave frequency 33.98 GHz, modulation frequency 12 kHz, modulation amplitude 0.45 mT. (a,b) Best simulation obtained by considering only the exchange interaction with $|J_{mp}| = 1.2 \times 10^{-3}$ cm^{-1}. The spectrum was calculated by using the *g* values and line width parameters given in Table 1. (c,d) Best simulation obtained by introducing the dipolar interactions with Fe_1 = Fe(III) and the sets of parameters given in Tables 1 and 2. (e,f) Best simulation obtained by introducing the dipolar interactions with Fe_1 = Fe(II) and the set of parameters given in Tables 1 and 2.

Table 2: Parameters Used in the Numerical Simulation of the Split Mo(V) Signal Shown in Figure 3 with the Two Assignments Fe_1 = Fe(III) and Fe_1 = Fe(II)

	α	β	γ	*a*	*b*	*c*	J_{mp} (cm^{-1})
Fe_1 = Fe(III)	90	0	0	313	32	97	-1.2×10^{-3}
Fe_1 = Fe(II)	0[a]	90[a]	0[a]	180[a]	50[a]	180[a]	$+1.2 \times 10^{-3}$
	90	0	0	225	60	40	-1.2×10^{-3}
	0	0	0	30	55	145	-1.2×10^{-3}
	0	90	90	355	70	224	$+1.2 \times 10^{-3}$
	90	90	0	23	55	42	$+1.2 \times 10^{-3}$
	90	90	90	346	122	42	$+1.2 \times 10^{-3}$

[a] With Fe_1 = Fe(II), the best fit shown in Figure 3ef was obtained with this set, but almost equivalent fits were obtained with the other sets of parameters.

3d,f), they could be discriminated at lower frequency (X-band) where the effect of the spin−spin interactions is comparatively stronger (Figure 3c,e). The position and the relative amplitude of the spectral features were best reproduced with Fe_1 = Fe(II). In all calculated spectra, the effect of the spin−spin interactions was barely detectable in signal I.

Spin−Spin Interactions between the Proximal and Distal [2Fe-2S]$^{1+}$ Centers of D.gigas AOR. At X-band, these interactions are manifested in signal I by a splitting of the $g_z = 2.020$ peak and a broadening of the g_x, g_y region (Figure 4a). No effect is seen in the much broader signal II. The Q-band spectrum is identical to that obtained without interaction (Figures 2d and 4b). No acceptable fit of the split signal I could be obtained by considering only the exchange term $J_{pd}\mathbf{S}_p\cdot\mathbf{S}_d$. The dipolar terms were introduced by using the valences {Fe_1 = Fe(II), Fe_2 = Fe(III)} deduced previously, with the two possible assignments Fe_3 = Fe(II) and Fe_3 = Fe(III). For each of these assignments, the 6 orientations of the $\mathbf{g}_p$ tensor with respect to (*X*, *Y*, *Z*) and the 6 orientations of the $\mathbf{g}_d$ tensor with respect to (*X*′, *Y*′, *Z*′) were tested. For each of these 72 configurations, a single adjustable

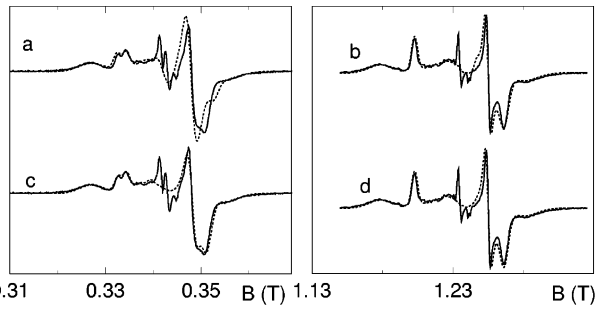

FIGURE 4: Interaction spectrum displayed at X- and Q-bands by the proximal and distal [2Fe-2S]$^{1+}$ centers of *D. gigas* AOR. Experimental conditions: X-band, temperature 8 K, microwave frequency 9.4309 GHz, power 10 μW, modulation frequency 2.9 kHz, modulation amplitude 0.5 mT; Q-band, temperature 30 K, microwave frequency 33.98 GHz, power 35 μW, modulation frequency 10 kHz, modulation amplitude 1 mT. (a,b) Best simulation obtained with Fe_3 = Fe(III) and the set of parameters given in Tables 1 and 3. (c,d) Best simulation obtained by introducing the dipolar interactions with Fe_3 = Fe(II) and the set of parameters given in Tables 1 and 3.

Table 3: Parameters Used in the Numerical Simulation of the Split Signal I Shown in Figure 4 with the Two Assignments Fe_3 = Fe(III) and Fe_3 = Fe(II)

	α	β	γ	α¢	β¢	γ¢	J_{pd} (cm^{-1})
Fe_3 = Fe(III)	90	90	90	90	90	0	$+4.2 \times 10^{-4}$
Fe_3 = Fe(II)	0[a]	90[a]	0[a]	0[a]	90[a]	0[a]	-8.2×10^{-4}
	0	90	0	0	90	90	-8.3×10^{-4}
	0	90	0	90	90	90	-8.3×10^{-4}
	0	90	90	0	0	0	-7.1×10^{-4}
	0	90	90	0	90	0	-8.2×10^{-4}
	0	90	90	0	90	90	-8.3×10^{-4}
	0	90	90	90	90	0	-6.9×10^{-4}
	0	90	90	90	90	90	-8.5×10^{-4}

[a] With Fe_3 = Fe(II), the best fit shown in Figure 4c,d was obtained with this set, but equivalent fits were obtained with the other sets of parameters.

parameter, the exchange parameter J_{pd}, was involved in the fitting procedure. With Fe_3 = Fe(III), the two Fe(III) ions are separated by the shortest iron-to-iron distance of 12.2 Å, so that the effect of the dipolar interactions is maximum. No acceptable fit could be obtained with this assignment regardless of the orientation of the **g** tensors (Figure 4a,b). In contrast, good fits were obtained for various orientations of the **g** tensors with Fe_3 = Fe(II) by using negative values of J_{pd} (Table 3). The best fit, which was given by the sets ($\alpha = 0°$, $\beta = 90°$, $\gamma = 0°$), ($\alpha' = 0°$, $\beta' = 90°$, $\gamma' = 0°$), and $J_{pd} = -8.2 \times 10^{-4}$ cm^{-1}, is shown in Figure 4c,d. We have seen previously that the set ($\alpha = 0°$, $\beta = 90°$, $\gamma = 0°$) also provides a good simulation of the split Mo(V) signal (Table 2). For this orientation, the magnetic axis corresponding to the largest *g* value is perpendicular to the iron-to-iron direction. This orientation differs from that predicted by a simple ligand field model (*26*), but is close to those deduced from an ENDOR study carried out on a plant-type ferredoxin (*27*) and from a recent density functional theory calculation (*28*). Since the (α, β, γ, α', β', γ') values were not varied continuously, our study does not bring a definite conclusion about the direction of the magnetic axes in [2Fe-2S]$^{1+}$ clusters. However, it clearly demonstrates that the reducible iron sites of the proximal and distal centers are Fe_1 coordinated to Cys 100 and Cys 139, and Fe_3 coordinated to Cys 40 and Cys 45, respectively.

Spin−Spin Interactions between the Mo(V) Center and the Proximal [2Fe-2S]$^{1+}$ Center of Milk Xanthine Oxidase. Although the arrangement of the metal centers in milk xanthine oxidase is very similar to that found in *D. gigas* AOR (*5*), the effect of the spin−spin interactions is visible only in the Mo(V) signal (*17*). The method used in the case of *D. gigas* AOR was applied to the numerical simulation of the split slow-type Mo(V) signal displayed by the desulfo-inhibited form of milk xanthine oxidase. The *g* values and line width parameters of this signal and of signal I have been determined in a previous work (*18*). The Mo−Fe distances needed in the calculation were taken from the 2.5 Å resolution crystal structure (*5*). As in the case of *D. gigas* AOR, the main features of the X-band and Q-band Mo(V) split signal could be reproduced by considering only the exchange term $J_{mp}\mathbf{S}_m\cdot\mathbf{S}_p$ of the spin−spin interactions with $|J_{mp}| = 2.2 \times 10^{-3}$ cm^{-1} (Figure 5a,b). The dipolar terms were then introduced with the two possible assignments Fe_1 = Fe(III) and Fe_1 = Fe(II). In the former case, no acceptable fit could be obtained whatever the orientation of the $\mathbf{g}_m$ and $\mathbf{g}_p$ tensors (Figure 5c,d). With Fe_1 = Fe(II), the best fit was obtained with a negative J_{mp} value and the same orientation of the $\mathbf{g}_p$ tensor ($\alpha = 0°$, $\beta = 90°$, $\gamma = 0°$) as in the case of *D. gigas* AOR (Figure 5e,f). Although the fit was significantly improved by introducing the dipolar terms, it was poorer than that obtained in the case of *D. gigas* AOR (Figures 3e,f and 5e,f). The assignment Fe_1 = Fe(II) differs from that obtained in a similar work which was carried out before the structure of the enzyme was known (*18*). This demonstrates that, when the dipolar interactions are weak, the knowledge of the protein structure is needed to enable an unambiguous assignment of the valences of the iron ions.

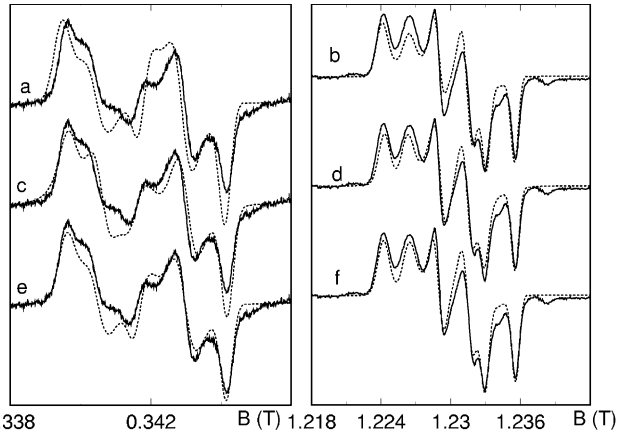

FIGURE 5: Split slow-type Mo(V) signal of milk xanthine oxidase recorded at X- and Q-bands. Experimental conditions: X-band, temperature 40 K, microwave frequency 9.4312 GHz, power 10 μW, modulation frequency 2.9 kHz, modulation amplitude 0.05 mT; Q-band, temperature 30 K, microwave frequency 33.94 GHz, power 4.3 μW, modulation frequency 10 kHz, modulation amplitude 0.2 mT. (a,b) Best simulation obtained by considering only the exchange interaction with $|J_{mp}| = 2.2 \times 10^{-3}$ cm^{-1}. (c,d) Best simulation obtained by introducing the dipolar interactions with Fe_1 = Fe(III) and $\alpha = 90°$, $\beta = 0°$, $\gamma = 0°$, $J_{mp} = 2.1 \times 10^{-3}$ cm^{-1}. (e,f) Best simulation obtained by introducing the dipolar interactions with Fe_1 = Fe(II) and $\alpha = 0°$, $\beta = 90°$, $\gamma = 0°$, $J_{mp} = -2.2 \times 10^{-3}$ cm^{-1}.

DISCUSSION

Valence Assignment. To our knowledge, the identification of the reducible site of the [2Fe-2S] clusters of molybdenum hydroxylases has not yet been reported in the literature. In these proteins, the distal center is coordinated by the C−X_4−C−X_2−C−X_n−C cysteine motif found in plant-type ferredoxins and in a number of redox enzymes. The various methods used to identify the reducible site in clusters bound by this motif have yielded consistent results. NMR studies have first established that the reducible iron site is that coordinated by the first two cysteines in plant-type ferredoxins (*29*). In the case of the [2Fe-2S] cluster of the FrdB subunit of *Escherichia coli* fumarate reductase, the same assignment was obtained by exploiting the different sensitivity of the EPR spectrum toward Cys-to-Ser substitutions affecting the ferrous and ferric sites (*30*). The same assignment was also deduced from the study of spin−spin interactions in the case of the [2Fe-2S] center of the phthalate dioxygenase reductase of *P. cepacia* (*24*) and of the distal center of *D. gigas* AOR in the present work. Taken together, these results suggest that the location of the reducible site of [2Fe-2S] clusters coordinated by this cysteine motif is fully determined by the arrangement of the cysteines. In contrast, the magnetic characteristics of these clusters, like the *g* values and the exchange parameter, which are sensitive to subtle structural details, can vary greatly (*31*).

Few data concerning [2Fe-2S] clusters coordinated by other cysteine motifs have been reported in the literature. The [2Fe-2S] cluster of human ferredoxin, the human equivalent of bovine adrenodoxin, is coordinated by cysteines 46, 52, 55, and 92, which is a very similar motif to that found in plant ferredoxins. Thus, the finding that the effect of Cys-to-Ser substitutions on the EPR spectrum is consistent with the reducible iron site being coordinated by Cys 46 and Cys 52 in this protein was not really surprising (*31*). A very different situation is found in the case of the [2Fe-2S] ferredoxin from *Clostridium pasteurianum* where the cluster is coordinated by cysteines 11, 24, 56, and 60. In this case, the EPR data concerning Cys-to-Ser mutants have shown that the reducible site is coordinated by Cys 56 and Cys 60 (*32*). [2Fe-2S] clusters coordinated by the same cysteine motif are found in other [2Fe-2S] ferredoxins. A recent study has shown that, in these ferredoxins, the magnitude of the exchange interaction between the two Fe ions of the cluster can vary greatly (*33*).

The C−X_2−C−X_n-C−X−C motif coordinating the proximal [2Fe-2S] cluster of molybdenum hydroxylases, and the entire structure of the domain containing this cluster, are unique among iron−sulfur proteins. Our study indicates that the reducible site of this cluster is coordinated by the first and fourth cysteines in *D. gigas* AOR. We have seen that the same assignment is obtained in milk xanthine oxidase when the split Mo(V) spectrum is simulated by using the arrangement of the metal centers given by the crystal structure (Figure 5). Independent support for the reducible sites being identical in xanthine oxidase and in *D. gigas* AOR comes from a reanalysis of Cys-to-Ser substitution experiments carried out in rat xanthine oxidase (*22*). In this protein, the distal and proximal clusters are coordinated by cysteines 43, 48, 51, 72 and cysteines 112, 115, 147, 149, respectively. Signal I is characterized by *g* values equal to 1.90, 1.93, 2.02, and signal II is of the unusual type, with *g* values estimated at 1.90, 2.00, 2.11 ($g_{av} \approx 2.00$). Neither signal I nor signal II was appreciably modified in the C51S mutant. In the C43S mutant, signal I was not modified but signal II

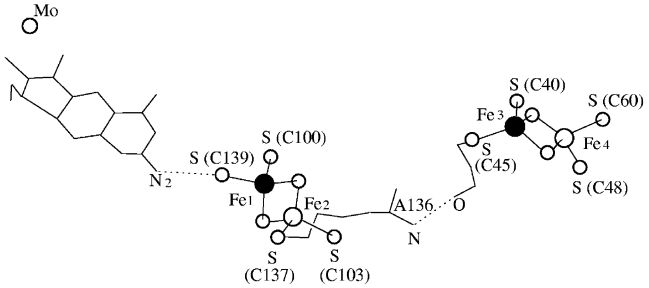

FIGURE 6: Relative arrangement of the metal centers given by the X-ray crystal structure of *D. gigas* AOR. The reducible iron sites determined in this work are marked as filled circles, and the electron-transfer pathways proposed in ref 2 are shown. The exchange parameters deduced from the study are $J_{md} = +1.2 \times 10^{-3}$ cm^{-1} for the interactions between the Mo(V) center and the proximal [2Fe-2S]$^{1+}$ center and $J_{pd} = -8 \times 10^{-4}$ cm^{-1} for the interactions between the two [2Fe-2S]$^{1+}$ clusters.

was converted to a usual type signal with g values equal to 1.93, 1.94, 2.05 ($g_{av} \approx 1.97$). When Cys 115 ligating the proximal center was substituded by Ser, signal II was essentially unchanged but the g values of signal I were slightly shifted to 1.90, 1.91, 2.01. These results were interpreted by the authors in terms of signals I and II arising from the proximal and distal clusters, respectively (*22*). Moreover, these results indicate that the ferric and ferrous sites of the distal center are bound to Cys 51 and Cys 43, respectively. They also strongly suggest that the ferric site of the proximal center is bound to Cys 115. These assignments are identical to those obtained in the present study.

Electron Transfers and Exchange Interactions. The location of the reducible sites of the FeS centers found in the present work is shown in Figure 6. We have also represented the electron-transfer pathways proposed on the basis of the crystal structure of *D. gigas* AOR (*2*, *14*). The first pathway connects the molybdenum cofactor to the reducible site of the proximal center through the hydrogen bond between the N2 atom of the pterin ring and the sulfur atom of Cys 139. The second pathway connects the ferric site of the proximal center to the reducible site of the distal center through Cys 137, Ala 136, and the hydrogen bond between the peptide nitrogen of Ala 136 and the peptide oxygen of Cys 45. Although interpreting electron-transfer processes in terms of a single pathway is probably simplistic, the picture shown in Figure 6 is reasonable because the metal sites which are directly connected are also the nearest. The location of the reducible site of the proximal cluster appears favorable for an efficient transfer from the molybdenum center, but the reducible sites of the proximal and distal clusters are not directly connected (Figure 6). However, this is not expected to prevent a fast transfer between the two FeS clusters. It should be recalled that, upon reduction of a [2Fe-2S]$^{2+}$ cluster, the added electron is essentially distributed between the bridging sulfur atoms and the thiolate groups of the reducible site, but the charge carried by the thiolate groups of the "nonreducible site" is also significantly decreased (*34*). Since the distal cluster is exposed to the solvent via Cys 60 which is a ligand of the "nonreducible" site, the same remarks might apply to the transfer to the external electron acceptor.

Although long-range ferromagnetic and antiferromagnetic interactions between metal centers have been reported for a long time (*35*), few data are available in the case of metal centers in proteins. Since the electron-transfer pathways shown in Figure 6 are expected to mediate the exchange interactions between the paramagnetic sites of the system, they can help analyze the values of the exchange parameters J_{mp} and J_{pd} deduced from the study of the spin−spin interactions. The set of Euler angles ($\alpha = 0°$, $\beta = 90°$, $\gamma = 0°$) which provides the best simulations of both the split Mo(V) signal and the split signal I is associated with a positive J_{mp} value (Table 2). This parameter can be written $J_{mp} = {}^{7}/_{3}J(m,\mathrm{III}) - {}^{4}/_{3}J(m,\mathrm{II})$, where $J(m,\mathrm{III})$ and $J(m,\mathrm{II})$ describe the exchange interactions between the Mo(V) center and the ferric and ferrous sites of the proximal [2Fe-2S]$^{1+}$ cluster, respectively (*18*). According to the scheme shown in Figure 6, the dominant term is $J(m,\mathrm{II})$ which is therefore expected to be negative, corresponding to a ferromagnetic interaction. We now consider J_{pd} which is determined by the exchange interactions between the four iron sites of the proximal and distal [2Fe-2S]$^{1+}$ centers. Since these interactions are mainly mediated by the pathway involving Cys 137, Ala 136, and Cys 45 (Figure 6), J_{pd} is expected to be equal to $(-28/9)\ J(\mathrm{III,II})$ (*18*), where $J(\mathrm{III,II})$ describes the interaction between the ferric site of the proximal cluster and the ferrous site of the distal center. The negative J_{pd} values deduced from the study of the spin−spin interactions between the two FeS clusters (Table 2) are therefore indicative of a positive $J(\mathrm{III,II})$ value, corresponding to an antiferromagnetic interaction.

The efficiency of electron-transfer systems is sometimes evaluated by using semiquantitative methods (*36*, *37*). This requires that the border between the redox cofactors and the protein is properly defined, and this is not straightforward in the case of simple mononuclear metal centers (*38*). This is even more difficult for *D. gigas* AOR in which the spatial extent of the cofactors is comparable to the center-to-center distances (Figure 6). Since J_{mp} and J_{pd} are of the same magnitude, the electronic factors for the electron transfers between the Mo center and the proximal [2Fe-2S] cluster and between the two [2Fe-2S] clusters are expected to be similar. Actually, a quantitative relationship between the exchange parameter and the electronic factor may exist when there is a single unpaired electron on each redox site (*39*, *40*). This relationship was successfully applied to kinetic data obtained for several diradical pairs (*40*−*42*), but the agreement was found to be only qualitative in the case of mixed-valence Ru(III)−Ru(II) complexes and of 2[4Fe-4S] ferredoxins (*43*, *44*). It will be especially interesting to apply this relationship to the electron-transfer chain of *D. gigas* AOR as soon as kinetic data are available.

CONCLUDING REMARKS

The present work shows that the valences of the metal sites of biological polynuclear centers can be determined through the quantitative study of their spin−spin interactions based on the X-ray crystal structure. In the case of AOR, which is a three-center system, the analysis was facilitated by the structural arrangement of the centers and by the very different line widths of their EPR signals. In particular, the spin−spin interactions between the Mo center and the proximal [2Fe-2S]$^{1+}$ cluster are manifested only in the Mo(V) signal and the splitting of signal I comes from the spin−spin interactions between the two [2Fe-2S]$^{1+}$ clusters.

The situation is less favorable in the case of other molybdenum hydroxylases for which no splitting due to

spin−spin interactions is apparent in the EPR spectrum despite a very similar arrangement of the metal centers. Besides *D. gigas* AOR and xanthine oxidase, the split Mo(V) signal has been reported only in the case of *Pseudomonas carboxydovorans* CO dehydrogenase (*45*) and of *Desulfovibrio alaskensis* (*21*). Indeed, observation of this signal requires special conditions. The desulfo form of the enzyme must be reduced in ^2H_2O, and the EPR spectrum must be recorded at low temperatures with a nonsaturating microwave power and a small modulation amplitude. This could explain why a split Mo(V) signal was not detected in some studies. Likewise, the split signal I was observed only in the case of *D. gigas* AOR, *D. alaskensis* AOR (*21*), and isoquinoline 1-oxidoreductase from *Pseudomonas diminuta* (*12*). Although no splitting is visible in the case of xanthine oxidase, the g_z peak of signal I recorded at X-band seems to be broader at 15 K than at 55 K (*46*). Since this spectrum arose from a sample containing very little Mo(V) species, this low-temperature broadening could be due to the spin−spin interactions between the two FeS clusters. Nevertheless, the effect of these interactions on the EPR spectrum is very different in the case of *D. gigas* AOR and of xanthine oxidase. The results obtained in the present work, together with the analysis of Cys-to-Ser substitution experiments carried out in rat xanthine oxidase (*22*), indicate that the location of the ferric and ferrous sites of the $[2Fe\text{-}2S]^{1+}$ clusters are identical in these enzymes. Moreover, the g values and the line widths of the various features of signal I are similar in both enzymes. Therefore, the difference between the effect of the spin−spin interactions may come from the exchange parameter J_{pd} and from the tensor $\mathbf{g}_d$ of the distal center whose principal values differ significantly in xanthine oxidase and in *D. gigas* AOR. Although further studies are needed to clarify this point, it is worthwhile noting that the enzymes which do not display a split signal I contain a FAD domain. Since removal of this domain can affect the magnetic properties of the distal FeS center (*19*), this observation might be relevant.

REFERENCES

1. Hille, R. (1996) The mononuclear molybdenum enzymes, *Chem. Rev. 96*, 2757−2816.
2. Romao, M. J., Archer, M., Moura, I., Moura, J. J. G., Le Gall, J., Engh, R., Schneider, M., Hof, P., and Huber, R. (1995) Crystal structure of the xanthine oxidase-related aldehyde oxido-reductase from *D. gigas*, *Science 270*, 1170−1176.
3. Dobbek, H., Gremer, L., Meyer, O., and Huber, R. (1999) Crystal structure and mechanism of CO dehydrogenase, a molybdo iron-sulfur flavoprotein containing S-selenylcysteine, *Proc. Natl. Acad. Sci. U.S.A. 96*, 8884−8889.
4. Hänzelmann, P., Dobbek, H., Gremer, L., Huber, R., and Meyer, O. (2000) The effect of intracellular molybdenum in *Hydrogenophaga pseudoflava* on the crystallographic structure of the seleno-molybdo-iron-sulfur flavoenzyme carbon monoxide dehydrogenase, *J. Mol. Biol. 301*, 1221−1235.
5. Enroth, C., Eger, B. T., Okamoto, T., Nishino, T., and Pai, E. F. (2000) Crystal structures of bovine milk xanthine dehydrogenase and xanthine oxidase: structure-based mechanism of conversion, *Proc. Natl. Acad. Sci. U.S.A. 97*, 10723−10728.
6. Truglio, J. J., Theis, K., Leimkuhler, S., Rappa, R., Rajagopalan, K. V., and Kisker, C. (2002) Crystal structures of the active and alloxanthine-inhibited forms of xanthine dehydrogenase from *Rhodobacter capsulatus*, *Structure 10*, 115−125.
7. Nishino, T., and Okamoto, K. *J.* (2000) The role of the [2Fe-2S] cluster centers in xanthine oxidoreductase, *J. Inorg. Biochem. 82*, 43−49.
8. Olson, J. S., Ballou, D. P., Palmer, G., and Massey, V. (1974) The mechanism of action of xanthine oxidase, *J. Biol. Chem. 249*, 4363−4382.
9. Hille, R., and Anderson, R. F. (1991) Electron transfer in milk xanthine oxidase as studied by pulse radiolysis, *J. Biol. Chem. 266*, 5608−5615.
10. Hille, R., and Anderson, R. F. (2001) Coupled electron/proton transfer in complex flavoproteins: solvent kinetic isotope effect studies of electron transfer in xanthine oxidase and trimethylamine dehydrogenase, *J. Biol. Chem. 273*, 31193−31201
11. Parschat, K., Canne, C., Hüttermann, J., Kappl., R., and Fetzner, S. (2001) Xanthine dehydrogenase from *Pseudomonas putida* 86: specificity, oxidation-reduction potentials of its redox-active centers, and first EPR characterization, *Biochim. Biophys. Acta 1544*, 151−165.
12. Canne, C., Stephan, I., Finsterbusch, J., Lingens, F., Kappl, R., Fetzner, S., and Hüttermann, J. (1997) Comparative EPR and redox studies of three prokaryotic enzymes of the xanthine oxidase family: quinoline 2-oxidoreductase, quinaldine 4-oxidase, and isoquinoline 1-oxidoreductase, *Biochemistry 36*, 9780−9790.
13. More, C., Belle, V., Asso, M., Fournel, A., Roger, G., Guigliarelli, B., and Bertrand, P. (1999) EPR spectroscopy: a powerful technique for the structural and functional investigation of metalloproteins, *Biospectroscopy 5*, S3−S18.
14. Rebelo, J. M., Dias, J. M., Hüber, R., Moura, J. J. G., and Romao, M. J. (2001) Structure refinement of the aldehyde oxidoreductase from *Desulfovibrio gigas* (MOP) at 1.28 Å, *J. Biol. Inorg. Chem. 6*, 791−800.
15. Barata, B. A. S., Liang, J., Moura, I., Le Gall, J., Moura, J. J. G., and Huynh, B. H. (1992) Mossbauer study of the native, reduced and substrate-reacted *Desulfovibrio gigas* aldehyde oxido-reductase, *Eur. J. Biochem. 204*, 773−778.
16. Caldeira, J., Belle, V., Asso, M., Guigliarelli, B., Moura, I., Moura, J. J. G., and Bertrand, P. (2000) Analysis of the electron paramagnetic resonance properties of the $[2Fe\text{-}2S]^{1+}$ centers in molybdenum enzymes of the xanthine oxidase family: assignment of signals I and II, *Biochemistry 39*, 2700−2707.
17. Lowe, D. J., and Bray, R. C. (1978) Magnetic coupling of the molybdenum and iron-sulphur centres in xanthine oxidase and xanthine dehydrogenases, *Biochem. J. 169*, 471−479.
18. Bertrand, P., More, C., Guigliarelli, B., Fournel, A., Bennett, B., and Howes, B. (1994) Biological polynuclear clusters coupled by magnetic interactions: from the point dipole approximation to a local spin model, *J. Am. Chem. Soc. 116*, 3078−3086.
19. Gremer, L., Kellner, S., Dobbeck, H., Huber, R., and Meyer, O. (2000) Binding of flavin adenine dinucleotide to molybdenum-containing carbon monoxide dehydrogenase from *Oligotropha carboxidovorans*. Structural and functional analysis of a carbon monoxide dehydrogenase species in which the native flavoprotein has been replaced by its recombinant counterpart produced in *Escherichia coli*, *J. Biol. Chem. 275*, 1864−1872.
20. Canne, C., Lowe, D. J., Fetzner, S., Adams, B., Smith, A. T., Kappl, R., Bray, R. C., and Hüttermann, J. (1999) Kinetics and interactions of molybdenum and iron-sulfur centers in bacterial enzymes of the xanthine oxidase family: mechanistic implications, *Biochemistry 38*, 14077−14087.
21. Andrade, S. L. A., Brondino, C. D., Feio, M. J., Moura, I., and Moura, J. J. G. (2000) Aldehyde oxidoreductase activity in *Desulfovibrio alaskensis* NCIMB 13491: EPR assignment of the proximal [2Fe-2S] cluster to the Mo site, *Eur. J. Biochem. 267*, 2054−2061.
22. Iwasaki, T., Okamoto, K., Nishino, T., Mizushima, J., Hori, H., and Nishino, T. (2000) Sequence motif-specific assignment of two [2Fe-2S] clusters in rat xanthine oxidoreductase studied by site-directed mutagenesis, *J. Biochem. (Tokyo) 127*, 771−778.
23. Bertrand, P., Camensuli, P., More, C., and Guigliarelli, B. (1996) A local spin model to describe the magnetic interactions in biological molecules containing $[4Fe\text{-}4S]^{+}$ clusters. Application to Ni-Fe hydrogenases, *J. Am. Chem. Soc. 118*, 1426−1434.
24. Bertrand, P., More, C., and Camensuli, P. (1995) Evidence for a magic magnetic configuration between FMN and the [2Fe-2S]+ center of phthalate dioxygenase reductase of *Pseudomonas cepacia*, *J. Am. Chem. Soc. 117*, 1807−1809.
25. Turner, N., Barata, B., Bray, R. C., Deitung, J., Le Gall, J., and Moura, J. J. G. (1987) The molybdenum iron-sulphur protein from

Desulfovibrio gigas as a form of aldehyde oxidase, *Biochem. J. 243*, 755−761.
26. Bertrand, P., and Gayda, J.-P. (1979) A theoretical interpretation of the variations of some physical parameters within the [2Fe-2S] ferredoxin group, *Biochim. Biophys. Acta 579*, 107−121.
27. Canne, C., Ebelshäuser, M., Gay, E., Shergill, J. K., Cammack, R., Kappl, R., and Hüttermann, J. (2000) Probing magnetic properties of the reduced [2Fe-2S] cluster of the ferredoxin from *Arthrospira platensis* by 1H ENDOR spectroscopy, *J. Biol. Inorg. Chem. 5*, 514−526.
28. Gambarelli, S., and Mouesca, J.-M. (2004) Correlation between the magnetic g tensors and the local cysteine geometries for a series of reduced [2Fe-2S*] protein clusters. A quantum chemical density functional theory and structural analysis, *Inorg. Chem. 43*, 1441−1451.
29. Dugad, L. B., La Mar, G. D., Banci, I., and Bertini, I. (1990) Identification of localized redox states in plant-type two-iron ferredoxins using the nuclear Overhauser effect, *Biochemistry 29*, 2263−2271.
30. Werth, M. T., Cecchini, G., Mandori, A., Ackrell, B. A. C., Schröder, I., Gunsalus, R. P., and Johnson, M. K. (1990) Site-directed mutagenesis of conserved cysteine residues in *Escherichia coli* fumarate reductase: modification of the spectroscopic and electrochemical properties of the [2Fe-2S] cluster, *Proc. Natl. Acad. Sci. U.S.A. 87*, 8965−8969.
31. Guigliarelli, B., and Bertrand, P. (1999) Application of EPR spectroscopy to the structural and functional study of iron−sulfur proteins, *Adv. Inorg. Chem. 47*, 421−497.
32. Meyer, J., Fujinoka, J., Gaillard, J., and Lutz, M. (1994) Mutated forms of the [2Fe-2S] ferredoxin from *Clostridium pasteurianum* with noncysteinyl ligands to the iron-sulfur cluster, *Biochemistry 33*, 13642 650.
33. Dermoun, Z., De Lucas, G., Asso, M., Bertrand, P., Guerlesquin, F., and Guigliarelli, B. (2002) The NADP-reducing hydrogenase from *Desulfovibrio fructosovorans*: functional interaction between the C-terminal region of HndA and the N-terminal region of HndD subunits, *Biochim. Biophys. Acta 1556*, 217−2225.
34. Mouesca, J. M., Chen, J. L., Noodleman, L., Bashford, D., and Case, D. A. (1994) Density functional/Poisson−Boltzmann calculations of redox potentials for iron-sulfur clusters, *J. Am. Chem. Soc. 116*, 11898−11914.
35. Coffman, R. E., and Buettner, G. R. (1979) A limit function for long-range ferromagnetic and antiferromagnetic superexchange, *J. Phys. Chem. 83*, 2387−2392.
36. Beratan, D. N., Betts, J. N., and Onuchic, J. N. (1991) Protein electron transfer rates set by the bridging secondary and tertiary structure, *Science 252*, 1285−1288.
37. Moser, C. C., Keske, J. M., Warncke, K., Farid, R. S., and Dutton, P. L. (1992) Nature of biological electron transfer, *Nature 355*, 796−802.
38. Baum, R. M. (1993) Views on biological, long-range electron transfer stir debate, *Chem. Eng. News Feb. 22*, 20−23.
39. Bertrand, P. (1991) Application of electron transfer theories to biological systems, *Struct. Bonding 75*, 1−47.
40. Okamura, M. Y., Isaacson, R. A., and Feher, G. (1979) Spectroscopic and kinetic properties of the transient intermediate acceptor in reaction centers of *Rhodopseudomonas sphaeroides*, *Biochim. Biophys. Acta 546*, 394−417.
41. Calvo, R., Abresch, E. C., Bittl, R., Feher, G., Hofbauer, W., Isaacson, R. A., Lubitz, W., Okamura, M. Y., and Paddock, M. L. (2000) EPR study of the molecular and electronic structure of the semiquinone biradical $Q_A^{-\bullet}Q_B^{-\bullet}$ in photosynthetic reaction centers from *Rhodobacter sphaeroides*, *J. Am. Chem. Soc. 122*, 7327−7341.
42. Nelsen, S. F., Ismagilov, R. F., and Teki, Y. (1998) Comparison of the singlet, triplet energy gap of a symmetrical diradical dication with ET parameters derived from its optical spectrum, *J. Am. Chem. Soc. 120*, 2200−2201.
43. Aquino, M. A. S., Lee, F. L., Gabe, E. J., Bensimon, C., Greedan, J. E., and Crutchley, R. J. (1992) Superexchange metal-metal coupling in dinuclear pentaammineruthenium complexes incorporating a 1,4-dicyanamidobenzene dianion bridging ligand, *J. Am. Chem. Soc. 114*, 5130−5140.
44. Kümmerle, R., Gaillard, J., Kyritsis, P., and Moulis, J.-M. (2001) Intramolecular electron transfer in [4Fe-4S] proteins: estimates of the reorganization energy and electronic coupling in *Chromatium vinosum* ferredoxin, *J. Biol. Inorg. Chem. 6*, 446−451.
45. Bray, R. C., George, G. N., Lange, R., and Meyer, O. (1983) Studies by e.p.r. spectroscopy of carbon monoxide oxidases from *Pseudomonas carboxydovorans* and *Pseudomonas carboxydohydrogena*, *Biochem. J. 211*, 687−694.
46. Lowe, D., Lynden-Bell, R. M., and Bray, R. C. (1972) Spin-spin interaction between molybdenum and one of the iron-sulphur systems of xanthine oxidase and its relevance to the enzymic mechanism, *Biochem. J. 130*, 239−249.

BI0510025